A simplified model to estimate thermal resistance between carbon nanotube and sample in scanning thermal microscopy

OPEN ACCESS
IOP Publishing
Journal of Physics D: Applied Physics
J. Phys. D: Appl. Phys. **50** (2017) 494004 (8pp)
https://doi.org/10.1088/1361-6463/aa900e

A simplified model to estimate thermal resistance between carbon nanotube and sample in scanning thermal microscopy

Maxim Nazarenko[1,2], Mark C Rosamond[1,5], Andrew J Gallant[1,4], Oleg V Kolosov[3], Vladimir G Dubrovskii[2,4] and Dagou A Zeze[1,4,6]

[1] School of Engineering and Computing Sciences, Durham University, Durham DH1 3LE, United Kingdom
[2] St Petersburg Academic University, Khlopina 8/3, 194021 St Petersburg, Russia
[3] Department of Physics, Lancaster University, Lancaster LA1 4YB, United Kingdom
[4] University of Information Technologies, Mechanics and Optics, St. Petersburg, Russia

E-mail: d.a.zeze@durham.ac.uk

Received 3 July 2017, revised 18 September 2017
Accepted for publication 29 September 2017
Published 15 November 2017

Abstract

Scanning thermal microscopy (SThM) is an attractive technique for nanoscale thermal measurements. Multiwalled carbon nanotubes (MWCNT) can be used to enhance a SThM probe in order to drastically increase spatial resolution while keeping required thermal sensitivity. However, an accurate prediction of the thermal resistance at the interface between the MWCNT-enhanced probe tip and a sample under study is essential for the accurate interpretation of experimental measurements. Unfortunately, there is very little literature on Kapitza interfacial resistance involving carbon nanotubes under SThM configuration. We propose a model for heat conductance through an interface between the MWCNT tip and the sample, which estimates the thermal resistance based on phonon and geometrical properties of the MWCNT and the sample, without neglecting the diamond-like carbon layer covering the MWCNT tip. The model considers acoustic phonons as the main heat carriers and account for their scattering at the interface based on a fundamental quantum mechanical approach. The predicted value of the thermal resistance is then compared with experimental data available in the literature. Theoretical predictions and experimental results are found to be of the same order of magnitude, suggesting a simplified, yet realistic model to approximate thermal resistance between carbon nanotube and sample in SThM, albeit low temperature measurements are needed to achieve a better match between theory and experiment. As a result, several possible avenues are outlined to achieve more accurate predictions and to generalize the model.

Keywords: scanning thermal microscopy (SThM), multiwalled carbon nanotubes (MWCNT), interfacial resistance, Kapitza thermal resistance, nanoscale resolution scanning thermal microscopy

(Some figures may appear in colour only in the online journal)

[5] Now at the School of Electrical and Electronic Engineering, University of Leeds, Leeds LS2 9JT, United Kingdom.
[6] Author to whom any correspondence should be addressed.

1. Introduction

Nanotechnology is an umbrella term covering the study and manipulation of matter at the nanoscale. Well-developed and diverse techniques are required to achieve this efficiently. Atomic force microscopy (AFM) developed in 1986 [1] provides for both the study and manipulation of nanometer objects. A number of nanoscale microscopy techniques based on the AFM were developed throughout the years [2–8]. In particular, scanning thermal microscopy (SThM) investigates the thermal properties of materials at the nanoscale [9–13].

Currently, thermal management problems are some of the most significant limiting factors not only for high-power electric devices, but even more importantly, for high-speed electronic components [14–16]. As the characteristic device dimension shrinks while their thermal envelope remains roughly the same, the specific heat production is increased drastically. In order to optimize device design, astute measurement methods are required. Most current thermal measurement systems (such as infrared imaging, photoreflectance measurements, and Raman spectroscopy) are based on optical effects, limiting their resolution to micrometer scale [17–19]. SThM uses direct measurements techniques and allows for tens of nanometer spatial resolution. However, classical SThM techniques are not totally adequate for the study of high thermal conductivity materials such as semiconductors [20] due to their diminished ability to differentiate between such materials. Moreover, requirements for high spatial resolution, i.e. small contact area, inevitably result in a high thermal resistance, which, in turn, lowers thermal resolution even more.

This apparent contradiction may make the situation look hopeless. However, a possible mitigating approach is to use a high thermal conductivity element, such as multiwalled carbon nanotubes (MWCNT) to enhance the performance of the probe tip, in direct contact with the sample under study [21–25]. The outstanding geometric and mechanical properties, such as high aspect ratio, perfect crystalline structure and high Young's modulus [26] allow MWCNT to probe into deep and steep recesses and to flex while avoiding mechanical damage. If a relatively short conically shaped probe is used, similar to that explored later in this paper, the mechanical stability is unlikely to be compromised. In turn, the high thermal conductance due to the use of MWCNT may significantly improve the performance of SThM.

Early theoretical analysis confirmed the high potential of such an approach [25] that was then proven experimentally [24]. It is now reported in the literature that MWCNT may drastically increase spatial resolution while having sufficiently low thermal resistance as to keep required thermal sensitivity [24, 27]. However, the unique properties of MWCNT are coupled with new challenges. For instance, understanding the heat flow through the sample and probe remains a major challenge to achieve a better insight into thermal energy transport at the nanometer scale. It is also essential to simultaneously achieve the competing objective of high spatial resolution and high thermal sensitivity. This problem has many aspects, such as ballistic heat transport through the MWCNT [28, 29] and high anisotropy of the nanotube thermal conductivity. Here, we concentrate on the study of a significant component of the heat transfer in SThM, i.e. the ultimate interface between the MWCNT tip and the sample. The difference in material parameters gives rise to the so-called Kapitza thermal resistance [20]. Unlike bulk thermal resistance, Kapitza thermal resistance exists just at the interface between two different materials and does not depend on the thickness. Therefore, it makes a major contribution to thermal resistance of almost any nanoscale system. As such, the knowledge of the Kapitza resistance is crucial to the accurate measurement of materials thermal properties at the nanometer scale. It should be noted that there is very little literature on interfacial resistance involving carbon nanotubes under SThM configuration. For example, Hu *et al* [30] used molecular dynamics approach to study heat transport in CNT embedded in a matrix. Zhong *et al* [31] employed the same technique to investigate thermal resistance between overlapping CNTs, while Chalopin *et al* found significantly lower thermal conductivity of CNT pellets as compared to individual CNTs [32]. Mingo and Broido [29] studied ballistic heat transport in single-walled CNTs and found higher thermal resistance than thought earlier. While quite insightful, these studies do not directly address the research problem discussed in this paper.

An adequate interpretation of SThM measurements data requires one to account for interface thermal resistance. Unfortunately, direct experimental measurements of the Kapitza resistance are very challenging. Likewise, temperature change and phonon dispersion at the interface, temperature dependence measurements and current flow complicate further the prediction of the Kapitza resistance [33]. Moreover, most of the earlier studies, e.g. [34–37] consider bulk materials, where size effect are expected to play a significant role [28]. Here, we propose a simple theoretical model to estimate the thermal resistance at the interface between the MWCNT tip and the sample under study. Quantum consideration of the heat transfer is explored to account for the submicron lateral dimensions of MWCNTs. The model developed is subsequently compared with the experimental results available in the literature.

2. Methods: theoretical model

It is assumed that the main contribution to the heat transfer near and at the interface is due to bulk acoustic phonons [38, 39]. However, the theoretical model, as shown below, is not sensitive to the exact nature of heat carriers and can be expanded to consider other types of carriers. Moreover, generalization for two distinct types of carrier is possible, provided they do not influence each other's behavior.

An accurate definition of thermal resistance is rather complex, as detailed in the literature [33]. For instance, the need to consider the interfacial temperature discontinuity, current flow as well as temperature dependence measurements (i.e. realistic phonon dispersion and density of states (DoS) are required at higher temperatures in the acoustic diffusive model) makes the accurate prediction of the Kapitza resistance challenging. Therefore, the model proposed aims at

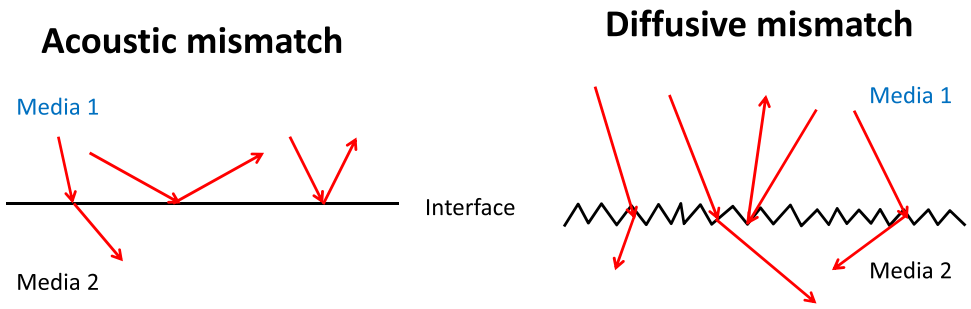

Figure 1. Two possible pathways of phonon scattering: acoustic mismatch, where phonons behave as planar waves (left) and diffuse mismatch, where all correlations at interface are completely destroyed (right). Possible phonon propagation paths are denoted by arrows.

offering a somewhat simplified, but still rigorous approach to address the problem outlined above by providing a realistic estimate of the Kapitza resistance. This requires a number of hypotheses described as follows.

Let us consider two macroscopic media 1 and 2 in thermal contact and each at a constant temperature T_1 and T_2, respectively. Let $\Theta_{12}^{\mathrm{tot}}$ be the total heat flux per unit area transported by all carriers arriving at the interface from medium 1 and passing into medium 2 (see figure 1). $\Theta_{12}^{\mathrm{tot}}$ accounts for all heat carriers having any possible energy. Likewise, $\Theta_{21}^{\mathrm{tot}}$ represents the total heat flux per unit area transported by all carriers arriving at the interface from medium 2 and passing into medium 1. Both fluxes are determined by the material parameters of the system and the temperature of the media which they originate from. The observable total heat flux from media 1 into media 2 is simply $\Theta_{12}^{\mathrm{tot}} - \Theta_{21}^{\mathrm{tot}}$, the interfacial thermal resistance ρ is then defined as:

$$\rho = \frac{T_1 - T_2}{\Theta_{12}^{\mathrm{tot}}(T_1) - \Theta_{21}^{\mathrm{tot}}(T_2)}. \tag{1}$$

Strictly speaking, the value of this interfacial resistance is governed by both the material system involved as well as temperatures T_1 and T_2, i.e. ρ is a function of both T_1 and $\Delta T = T_1 - T_2$.

Normally, when studying heat transfer on the macroscopic scale, we assume that the temperature changes abruptly at the interface. While that is a natural and useful idealization at the macroscale, it is not applicable at the nanoscale, where interface thickness may be of the same order of magnitude as the characteristic dimensions of other objects under study, and carriers are not fully thermalized. Therefore, we adopt a more careful continuous approach with no singularities in the temperature distribution.

As the system approaches thermal equilibrium (i.e. T_1 and T_2 approach a given value of T), the change of the interfacial resistance due to varying ΔT becomes smaller, until it becomes negligible. At the same time, $\Theta_{12}^{\mathrm{tot}}$ and $\Theta_{21}^{\mathrm{tot}}$ both approach an equivalent value Θ. In practical SThM measurement modes, a high degree of non-equilibrium is detrimental to accurate mapping of the thermal contrast between sample and probe, be it at low or high temperature. Relevant calibration is subsequently adopted to estimate contact resistance [13, 25]. Therefore, the thermal resistance at the interface may be calculated using equation (1):

$$\rho = \left(\frac{\partial \Theta_{12}^{\mathrm{tot}}(T)}{\partial T}\right)^{-1}. \tag{2}$$

The value of T_1 can be thought of as the temperature at the interface. Note also, that it makes no difference which of the fluxes, $\Theta_{12}^{\mathrm{tot}}$ or $\Theta_{21}^{\mathrm{tot}}$, is used in equation (2), since they are equal under the equilibrium state.

3. Results and discussion

3.1. Heat carriers scattering at the interface

The origin of the interface thermal resistance lies in the incident carrier being scattered at the interface. Normally, two pathways for phonon scattering are considered: the acoustic mismatch model, and the diffuse mismatch model [33]. The first one assumes that phonons are governed by continuum acoustics, i.e. phonons are considered as plane waves propagating in the continuous medium, while the interface is assumed perfectly planar. In the diffuse mismatch model, on the other hand, the opposite assumption is made: all the incident phonons are believed to be diffusely scattered at the interface, while correlations at interfaces are assumed to be completely destroyed by diffuse scattering. Hence, the transmission probability is defined solely by the principle of detailed balance and densities of phonon states. In other words, the probability that the phonon will scatter into a given side of the interface is totally independent of where the phonon came from. Instead, the probability of scattering into a given side is proportional to the density of phonon states on that side (Fermi's 'golden rule'). Those two mechanisms are illustrated in figure 1 left and right panels, respectively.

Since the interface between a SThM tip and the sample under study is generally rough on the nanometer and atomic scale, the diffuse mismatch model would be more appropriate: while the exact nature of phonon transport along the MWCNT comprises both diffusive and ballistic transport [13, 29], a phonon behavior at the interface, due to random reflections on irregularities, is assumed to depend solely on phonon energy. This assumption is reinforced by the experimental evidences of amorphous diamond-like carbon layer covering the MWCNT tip (figure 2). Therefore, the transmission probability p_{12} of a single phonon from the medium 1 to medium 2 depends on phonon's energy E, but not on its direction (by definition of

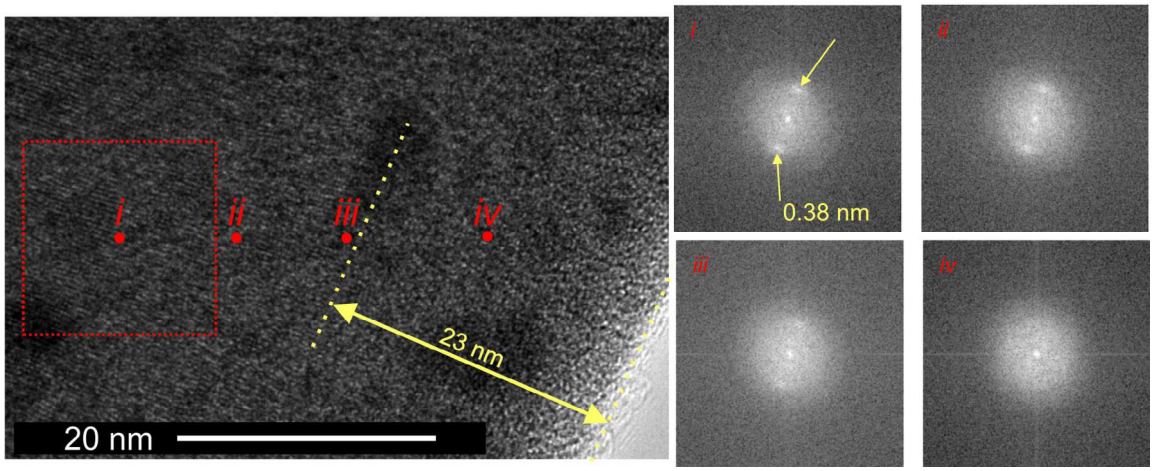

Figure 2. Close-up transmission electron microscopy (TEM) image of a MWCNT tip (left) and the equivalent diffraction patterns for each of the four regions (right).

the diffuse scattering): $p_{12} = p_{12}(E)$. Since the transmission probability does not depend on phonon polarization, the mode of the phonon is irrelevant in this case. Therefore, only one mode can be considered. In order to simplify the following calculations, Let $\Theta_{12}(E)$ be the heat flux carried by phonon having energy E going through the interface from medium 1 to medium 2 per unit area. From geometrical considerations, we have

$$\Theta_{12}(E) = \frac{1}{4\pi}\int_0^{2\pi} \mathrm{d}\phi \int_0^{\pi/2} \mathrm{d}\theta \sin(\theta)\cos(\theta)\, v_1(E)\, F_1(E,T)\, \sigma_1(E)\, p_{12}(E), \tag{3}$$

where $v_1(E)$ is the carrier propagation speed, $F_1(E,T)$ the occupation probability and $\sigma_1(E)$ the DoS, while subscript '1' denotes medium 1. An analytical expression is then obtained by solving the double integration shown in equation (3).

$$\Theta_{12}(E,T) = \frac{1}{4} v_1 F_1(E,T)\, \sigma_1(E)\, p_{12}(E). \tag{4}$$

The flux in the opposite direction is given by changing $1 \leftrightarrow 2$ in equation (4), where the subscript '2' denotes medium 2. The detailed balance consideration states that $\Theta_{12}(E) = \Theta_{21}(E)$ in equilibrium, yielding a relation between the p_{12} and p_{21}. Moreover, the diffusion scattering means that $p_{21}(E) = p_{11}(E)$, leading to the following relation for the transmission probability:

$$p_{12}(E) = \frac{v_2(E)\, F_2(E,T)\, \sigma_2(E)}{v_1(E)\, F_1(E,T)\, \sigma_1(E) + v_2(E)\, F_2(E,T)\, \sigma_2(E)}. \tag{5}$$

On the other hand, the *total* energy flux $\Theta_{12}^{\mathrm{tot}}$ transported by incident carriers arriving at the interface from medium 1 and passing into medium 2 is

$$\Theta_{12}^{\mathrm{tot}} = \frac{1}{4}\int E v_1(E)\, F_1(E,T)\, \sigma_1(E)\, p_{12}(E)\mathrm{d}E. \tag{6}$$

Substituting equation (6) into equation (2) leads to a general expression for the thermal interface resistance. For the case considered, a significant simplification can be made. Phonons in both media obey the Bose–Einstein statics with zero chemical potential, i.e. $F_1(E,T) = F_2(E,T) = (\exp(E/kT) - 1)^{-1}$. For a low energy, the propagation speed can be assumed to be constant. These considerations lead to the following final expression for the interface resistance:

$$\rho^{-1} = \frac{v_1 v_2}{4kT^2}\int \frac{\sigma_1(E)\, \sigma_2(E)\, E^2}{(v_1\sigma_1(E) + v_2\sigma_2(E))\sinh^2(E/2kT)}\mathrm{d}E. \tag{7}$$

In order to find a value of the contact thermal resistance, the DoS both in the sample and MWCNT tip must be calculated. This is performed using approach described below.

3.2. DoS in sample

For simplicity, a uniform substrate is considered where $\sigma_2(E) = \mathrm{d}V_k/\mathrm{d}E$, where V_k is the volume of a sphere containing all wavevectors smaller than k. For a 3D case, this results in

$$\sigma_2(E) = \frac{4\pi E^2}{\hbar^3 v_2^3}. \tag{8}$$

In turn, for a 2D sample with axial energy levels E_i, the density of state is as follows:

$$\sigma_2(E) = \frac{2\pi}{\hbar^2 v_2^2}\sum_{i\geqslant 1}(E - E_i)\, H(E - E_i), \tag{9}$$

where $H(x)$ is the Heaviside step function.

3.3. DoS in MWCNT

Based on the typical SEM images (figure 3), the MWCNT tip was modeled as an upside-down sharp truncated cone with a radius R:

$$R = R_0 + \kappa z, \tag{10}$$

where z is the axial coordinate counted from the small facet upwards, R_0 the MWCNT small facet radius, R the MWCNT radius at height z and κ the tangent of half of the taper angle ($\kappa = \tan(\alpha/2)$; figure 3).

Since phonons are confined in the MWCNT but free to travel within it, an infinite potential barrier at the boundary

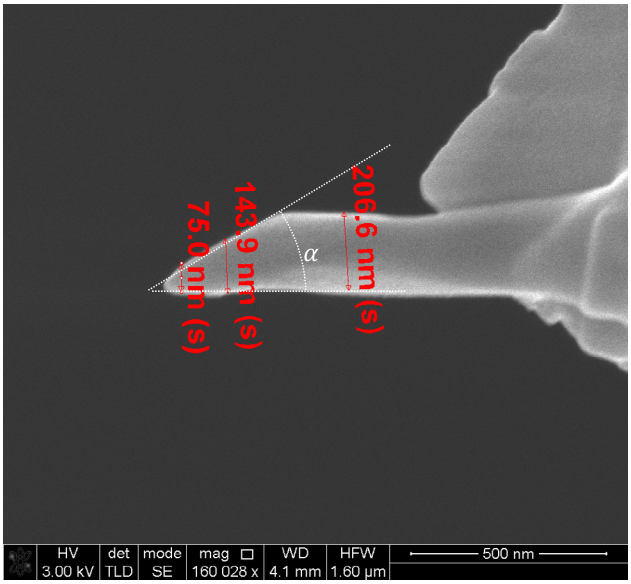

Figure 3. SEM of MWCNT as used to enhance a SThM probe tip; α is the taper angle.

with zero potential inside is assumed. Given an axial symmetry of the problem, cylindrical coordinates (r, ϕ, z) can be introduced, with z along the MWCNT axis. The Schrödinger equation associated with the phonons takes the form

$$-\frac{\hbar^2}{2m}\Delta\psi r\left(r,\phi,z\right) = E\psi\left(r,\phi,z\right), \tag{11}$$

with zero boundary conditions at the MWCNT boundary. To solve equation (11) for eigenvalues, the procedure detailed below was adopted. First of all, following the general particle-in-a-box method, the azimuthal contribution can be separated: $\psi\left(r,\phi,z\right) = \xi\left(r,z\right)\exp\left(\mathrm{i}k\phi\right)$. The equation for $\xi\left(r,z\right)$ than can be expressed in the usual for cylindrical coordinate system form

$$-\frac{\hbar^2}{2m}\frac{1}{\xi\left(r,z\right)}\left(\frac{1}{r}\frac{\partial}{\partial r}\left(r\frac{\partial}{\partial r}\right)+\frac{\partial^2}{\partial z^2}\right)\xi\left(r,z\right) = E - \frac{\hbar^2}{2mr^2}k^2. \tag{12}$$

Since boundary conditions mix radial and axial coordinates, further exact separation is impossible. Moreover, the electron diffraction pattern presented in figure 2 reveal an amorphous carbon layer which is about 23 nm thick, which results in phonons dispersion near the MWCNT tip being essentially isotropic. Therefore, high phonon anisotropy, typical for CNTs, is no longer valid for the interface region. To overcome this obstacle, we now employ the first order perturbation theory for the region of the taper angle. In order to do this, $\xi\left(r,z\right)$ can be represented as a product $\xi\left(r,z\right) = \eta(r)\zeta(z)$, where $\eta(r)$ has a weak z dependence due to the boundary conditions for r being dependent on z. In order to find $\eta(r)$ in the first approximation, equation (12) is first solved in the 0th approximation obtained under the assumption that $\kappa = 0$ and therefore, $\partial^2\eta(r)/\partial z^2 = 0$. Introducing z dependent boundary conditions would then results in $\partial^2\eta(r)/\partial z^2 \neq 0$. Finally, this derivative is substituted into equation (12) to find the first approximation to the solution. The individual key steps of this procedure are presented below.

The starting approximation for $\eta(r)$ is naturally $J_{|k|}\left(\lambda_{n,|k|}r/R\right)$, where $J_{|k|}$ is the Bessel function of the first kind with index $|k|$ and $\lambda_{n,|k|}$ is the nth zero of such a function. After substituting equation (10) into this expression, the second derivative of $\eta(r)$ is calculated and substituted into (12), resulting in the inhomogeneous equation

$$\begin{aligned}&\frac{1}{\eta(r)}\left(\frac{1}{r}\frac{\partial}{\partial r}\left(r\frac{\partial}{\partial r}\right)\right)\eta(r)\\&+\kappa^2\frac{1}{\eta(r)}\frac{\lambda_{n,|k|}^2}{R_0^4}\left[\left(R_0^2\frac{k^2-|k|}{\lambda_{n,|k|}^2}-r^2\right)J_{|k|}\left(\lambda_{n,|k|}\frac{r}{R_0}\right)+\frac{rR_0}{\lambda_{n,|k|}}J_{|k|+1}\left(\lambda_{n,|k|}\frac{r}{R_0}\right)\right]\\&+\frac{1}{\zeta(z)}\frac{\partial^2\zeta(z)}{\partial z^2} = -\frac{2mE}{\hbar^2}+\frac{k^2}{r^2}.\end{aligned} \tag{13}$$

Note that all the calculations are performed in the first order regarding κ^2. While equation (13) has multiple terms, it would allow for the separation of variables. Moreover, after the separation of variables, we obtain an inhomogeneous second order differential equation with respect to $\eta(r)$, which allows for an exact solution. While the initial solution may look unwieldy, it can be shown that it remains limited when $r \to 0$ at any k, i.e. no singularity was introduced due to approximation used. After simplification, the boundary condition $\eta\left(R\right) = 0$ can be written in the following form:

$$\begin{aligned}&J_{|k|}\left(\lambda R\right)\\&-\frac{\pi\kappa^2}{2}Y_{|k|}\left(\lambda_{n,|k|}\right)\int_0^{R_0}J_{|k|}\left(\lambda_{n,|k|}\frac{x}{R_0}\right)\left[\left(\frac{k^2-k}{R_0^2}-\frac{\lambda_{n,|k|}^2}{R_0^4}x^2\right)J_{|k|}\left(\lambda_{n,|k|}\frac{x}{R_0}\right)\right.\\&\left.+\frac{\lambda_{n,|k|}x}{R_0^3}J_{|k|+1}\left(\lambda_{n,|k|}\frac{x}{R_0}\right)\right]x\mathrm{d}x = 0.\end{aligned} \tag{14}$$

λ is the modified eigenvalue sought. By substitution, the integrand in equation (14) can be presented via dimensionless variable, finally obtaining

$$\begin{aligned}&J_{|k|}\left(\lambda R\right)-\frac{\pi\kappa^2}{2\lambda_{n,|k|}^2}Y_{|k|}\left(\lambda_{n,|k|}\right)\int_0^{\lambda_{n,|k|}}J_{|k|}(u)\left[\left(k^2-k-u^2\right)J_{|k|}(u)\right.\\&\left.+uJ_{|k|+1}(u)\right]u\mathrm{d}u = 0.\end{aligned} \tag{15}$$

Here, the integral can be calculated via hypergeometric functions. Denoting the whole second term in equation (15) as $\kappa^2 P$ leads to the first order approximation for the energy eigenvalue:

$$E = \frac{\hbar^2}{2mR_0^2}\left(\lambda_{n,|k|}^2-\kappa^2\frac{2P}{J_{|k|+1}\left(\lambda_{n,|k|}\right)}\right). \tag{16}$$

Note that in our approximation, the DoS for the radial component of the wave function scales perfectly with spatial dimensions, i.e. equation (15) depends on the MWCNT shape only as well as κ. The resulting DoS (obtained as a continuum approximation for the discrete energy spectrum) for a single axial mode is presented in figure 4.

The calculation of the total DoS takes into account the axial contribution; a typical result is shown in figure 5. The parameters used are directly related to the MWCNT shown in figure 3 and are discussed further below.

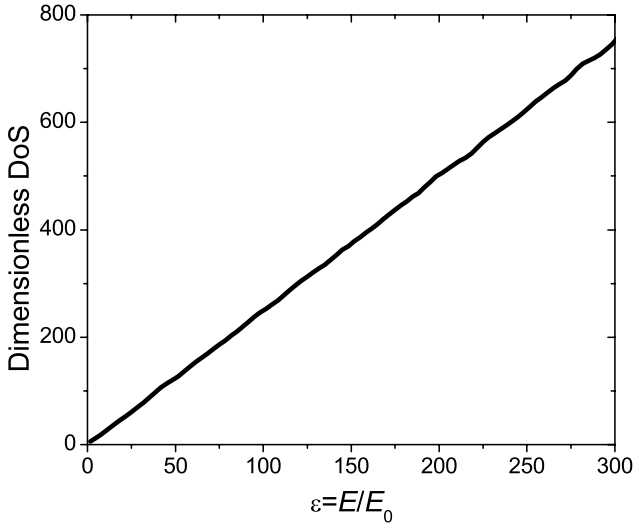

Figure 4. Dimensionless DoS versus dimensionless energy ($\varepsilon = E/E_0$) for a single axial mode. $E_0 \equiv \hbar^2/\left(2mR_0^2\right)$; dimensionless DoS is the number of possible states per dimensionless energy unit.

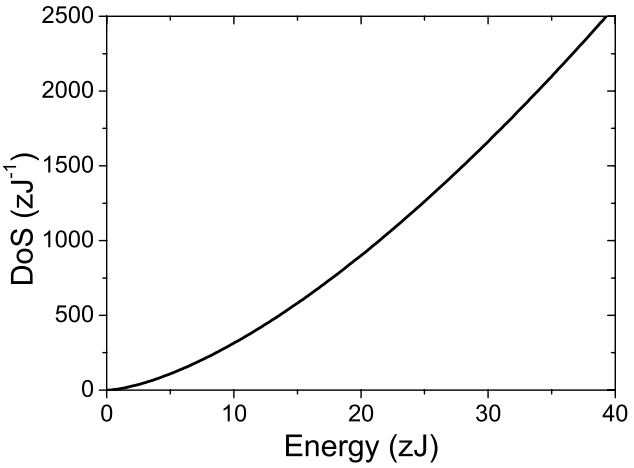

Figure 5. Total modified DoS for the MWCNT presented in figure 3.

Note that while the single mode DoS is mostly linear with some variations, the total DoS shows the expected close to quadratic shape.

3.4. Experimental verification

In order to validate our theoretical results, extensive experimental and theoretical considerations presented in [27] were used. The experimental results together with the heat conductance model allows for the estimation of the interface thermal resistance between MWCNT enhanced SThM tip and various materials. Timofeeva *et al* [27] found the value of the interface thermal resistance between MWCNT enhanced SThM tip and aluminum to be 5×10^{-9} K m^2 W^{-1} and between the same MWCNT enhanced SThM tip and 3 nm thick graphene flake to around 10^{-8} K m^2 W^{-1}. This value is noticeably higher than those found in [35, 36] for bulk graphene-metal interface,

Table 1. Interface thermal resistance values for MWCNT-Al and MWCNT-graphene.

Interface	MWCNT-Al K m^2 W^{-1}	MWCNT-graphene K m^2 W^{-1}
Theory	2.2×10^{-9}	4.2×10^{-9}
Experiment [27]	5.0×10^{-9}	1.0×10^{-9}

which illustrates the influence of MWCNT geometry on its properties. Interestingly [36] points out that phonon transport is indeed predominant at the interface, thus supporting our model. TEM images and the associated diffraction patterns displayed in figure 2 show the 23 nm thick amorphous carbon layer mentioned above and the transition from ordered structure with sp^2 hybridization (region I) to amorphous carbon (region IV). That means that the first 23 nm of the MWCNT from the tip are, in fact, amorphous, most likely the result of the structural modification induced by the cutting the MWCNT with a focused ion beam (heat load) during the SThM tip fabrication. This observation fully justifies the isotropic phonon model presented above.

To estimate speed of sound in MWCNT an average density 1300 kg m^{-3} and elastic modulus 63 GPa, were used the data of [40, 41]. This results in $v_1 \approx 7 \times 10^3$ m s^{-1}. For the aluminum substrate, the speed of sound was assumed to be 5×10^3 m s^{-1}. The base of the MWCNT appears to be larger than the tip apex. However, during the experiment, the contact pressure is high enough to ensure that the contact area on sample matches the MWCNT tip apex. After performing the steps outlined in the theoretical model, the final result for the interface thermal resistance was 2.2×10^{-9} K m^2 W^{-1}, which is close to the experimental results above. For the graphene substrate, the speed of sound to be 2.1×10^4 m s^{-1} was considered [42]. After repeating the same procedure, the interface thermal resistance was found to be around 4.2×10^{-9} K m^2 W^{-1}. This value is about two times lower than the experiment data for MWCNT-graphene interface resistance. This difference is most probably explained by an imperfect contact in the experimental setup. On the other hand, the value obtained for MWCNT-graphene is significantly higher than the thermal resistance between diamond-diamond (~7.3×10^{-9} K m^2 W^{-1}) and MgO-diamond (~7.5×10^{-9} K m^2 W^{-1}) reported in the literature [43]. This is attributable to the lower DoS in both MWCNT and graphene compared to that of bulk 3D materials, even though their acoustic properties are similar [44]. A summary of the results presented above are given in table 1.

The model proposed above relies on several assumptions which simplifies the calculation and remove the unknown phenomenological parameters. The deviations observed between experiment and theory may also be explained by the inherent assumptions of the model. For instance, the model predictions should be in better agreement with low temperatures experimental results which are not available. Likewise, an accurate estimation of temperature behavior at the interface at in the bulk material, as well as a realistic phonon dispersion and DoS will

also lead to a higher degree of agreement between experiment and theory. Finally, the effects of the probe-sample interface may include few monolayers of water that would be present even if only one of the contacting surfaces is hydrophilic.

Despite this, the model illustrates a realistic approximation which leads to relatively good fit between theoretical and experimental data. The current model deals only with one type of heat carriers, i.e. acoustic phonons, that is nevertheless appropriate for the CNT or graphene like materials where these are dominating thermal conductance. In addition, the model does not appear to strongly depend on the particular material composition of the probe. This suggests that more conventional materials such as Si_3N_4 can, in principle, be considered under the same framework, by virtue of their similar/comparable geometry. However, the overall thermal conductivity of the probe tips plays a significant performance role in the sensitivity and resolution of the SThM probe.

The model can be further improved to more involved theoretical constructions—if specific experiments can be designed to remove a few of the assumptions made, which is beyond the scope of this paper. Nevertheless, considering a different type of heat carriers, e.g. electrons or optical phonons, will mostly requires adjusting the DoS in the sample, since the heat carrier should obey the same Schrödinger equation in the MWCNT. In turn, accounting for several distinct heat independent carriers should be relatively straightforward, because the heat conductance is additive as long as carrier densities are low enough so that it does not result in an active carrier interaction. However, accounting for several distinct interacting heat carriers is more challenging. While the exact details depend heavily on the nature of the carriers, the perturbation technique might be used to approximate the equivalent Kapitza resistance.

From a theoretical standpoint, surface phonons might provide an interesting type of heat carrier. The surface DoS is normally much lower than that of the bulk, and the mean fee path of the carrier is also lower. Hence, the different behavior in the DoS from surface to bulk suggests a dissimilar dependence of thermal resistance on the probe geometry, i.e. for extremely thin probes (several nm), the contribution of surface phonons is likely to be significant.

4. Conclusion

We have developed a theoretical model capable of predicting, with a good approximation, the value of thermal resistance of the interface between a MWCNT and a specimen under study. The model accounts for the dimensions, geometrical shape of the MWCNT and the sample as well as the properties of the phonons. The model proposed is based on fundamental quantum properties of heat carriers in confined in MWCNT as well as universal thermodynamic considerations, which makes it a realistic approximation although the model can be enhanced further if combined iteratively with a systematic set of complex experiments.

Experimental validation of the model is challenging because of the difficulty to accurately measure SThM interface thermal resistance values. The actual contact area between the apex of the MWCNT tip and the sample is somewhat hard to measure accurately. However, the results predicted by the model are in fairly good agreement with published experimental data. This is illustrated by the interfacial thermal resistance values for bulk 3D aluminum and 2D graphene flake samples. For instance, the values predicted by the model, approximately 2×10^{-9} and 4×10^{-9} K m^2 W^{-1} for MWCNT-Al and MWCNT-graphene, interfaces, respectively, are of the same order of magnitude as the equivalent experimental data. If rather than with MWCNT, the probe is enhanced with a solid semiconductor nanorod [45], the model can also apply with an adjusted set of material parameters. However, it is important to note that the deviations between theory and experiment are essentially due to the boundary conditions applied to achieve a simplified model. In particular, building in the model, realistic estimates of the phonon dispersion and DoS, interfacial temperature behavior (all of which require extensive experimental data both at room and low temperature) will yield a higher agreement between theory and experiment.

Acknowledgments

This project has received funding from the European Union's Seventh Framework Programme (FP7) under the grant agreements: FUNPROB (GA-269169), NanoEmbrace (GA-316751), GRENADA (GA-246073) and QUANTIHEAT (GA-604668). We also acknowledge the support from the EPSRC grants EP/G015570/1 and EP/G017301/1, EPSRC-NSF grant EP/G06556X/1. DAZ thanks the Royal Academy of Engineering/LeverHulme Trust for the award of a Senior Research Fellowship. VGD thanks the Ministry of Education and Science of the Russian Federation for financial support under grant 14.587.21.0040 (project ID RFMEFI58717X0040).

ORCID iDs

Oleg V Kolosov https://orcid.org/0000-0003-3278-9643
Dagou A Zeze https://orcid.org/0000-0002-6596-5490

References

[1] Binnig G, Quate C F and Gerber C 1986 Atomic force microscope *Phys. Rev. Lett.* **56** 930
[2] Kaiser W and Bell L 1988 Direct investigation of subsurface interface electronic structure by ballistic-electron-emission microscopy *Phys. Rev. Lett.* **60** 1406
[3] Zhang L, Sakai T, Sakuma N, Ono T and Nakayama K 1999 Nanostructural conductivity and surface-potential study of low-field-emission carbon films with conductive scanning probe microscopy *Appl. Phys. Lett.* **75** 3527
[4] Nonnenmacher M, O'Boyle M P and Wickramasinghe H K 1991 Kelvin probe force microscopy *Appl. Phys. Lett.* **58** 2921
[5] Chang A M, Hallen H D, Harriott L, Hess H F, Kao H L, Kwo J, Miller R E, Wolfe R, van der Ziel J and Chang T Y 1992 Scanning Hall probe microscopy *Appl. Phys. Lett.* **61** 1974
[6] Matey J R and Blanc J 1985 Scanning capacitance microscopy *J. Appl. Phys.* **57** 1437

[7] Roelofs A, Böttger U, Waser R, Schlaphof F, Trogisch S and Eng L M 2000 Differentiating 180° and 90° switching of ferroelectric domains with three-dimensional piezoresponse force microscopy *Appl. Phys. Lett.* **77** 3444
[8] Hartmann U 1988 Magnetic force microscopy: some remarks from the micromagnetic point of view *J. Appl. Phys.* **64** 1561
[9] Duvigneau J, Schönherr H and Vancso G J 2010 Nanoscale thermal AFM of polymers: transient heat flow effects *ACS Nano* **4** 6932
[10] Puyoo E, Grauby S, Rampnoux J-M, Rouvière E and Dilhaire S 2011 Scanning thermal microscopy of individual silicon nanowires *J. Appl. Phys.* **109** 024302
[11] Klemens P G 2001 Theory of thermal conduction in thin ceramic films *Int. J. Thermophys.* **22** 265
[12] Gmelin E, Fischer R and Stitzinger R 1998 Sub-micrometer thermal physics—an overview on SThM techniques *Thermochim. Acta* **310** 1–17
[13] Pumarol M E, Rosamond M C, Tovee P, Petty M C, Zeze D A, Falko V and Kolosov O V 2012 Direct nanoscale imaging of ballistic and diffusive thermal transport in graphene nanostructures *Nano Lett.* **12** 2906–11
[14] Frank D J 2002 Power-constrained CMOS scaling limits *IBM J. Res. Dev.* **46** 235
[15] Borkar S 1999 Design challenges of technology scaling *IEEE Micro* **19** 23
[16] Beausoleil R G 2011 Large-scale integrated photonics for high-performance interconnects *J. Emerg. Technol. Comput. Syst.* **7** 6
[17] Soudi A, Dawson R D and Gu Y 2011 Quantitative heat dissipation characteristics in current-carrying GaN nanowires probed by combining scanning thermal microscopy and spatially resolved Raman spectroscopy *ACS Nano* **5** 255
[18] Kim K, Chung J, Hwang G, Kwon O and Lee J S 2011 Quantitative measurement with scanning thermal microscope by preventing the distortion due to the heat transfer through the air *ACS Nano* **5** 8700
[19] Kim K, Jeong W, Lee W and Reddy P 2012 Ultra-high vacuum scanning thermal microscopy for nanometer resolution quantitative thermometry *ACS Nano* **6** 4248
[20] Jeong T, Zhu J-G, Chung S and Gibbons M R 2012 Thermal boundary resistance for gold and CoFe alloy on silicon nitride films *J. Appl. Phys.* **111** 083510
[21] Hirotani J, Amano J, Ikuta T, Nishiyama T and Takahashi K 2013 Carbon nanotube thermal probe for quantitative temperature sensing *Sensors Actuators* A **199** 1–8
[22] Hirotani J, Ikuta T, Nishiyama T and Takahashi K 2011 Thermal boundary resistance between the end of an individual carbon nanotube and a Au surface *Nanotechnology* **22** 315702
[23] Holmes W, Gildemeister J M, Richards P L and Kotsubo V 1998 Measurements of thermal transport in low stress silicon nitride films *Appl. Phys. Lett.* **72** 2250
[24] Tovee P D, Rosamond M C, Pumarol M E, Jones R, Zeze D A, Petty M C and Kolosov O V 2014 Nanoscale resolution scanning thermal microscopy via carbon nanotube tipped thermal probes *Phys. Chem. Chem. Phys.* **16** 1174
[25] Tovee P, Pumarol M, Zeze D, Kjoller K and Kolosov O 2012 Nanoscale spatial resolution probes for scanning thermal microscopy of solid state materials *J. Appl. Phys.* **112** 114317
[26] Treacy M M J, Ebbesen T W and Gibson J M 1996 Exceptionally high Young's modulus observed for individual carbon nanotubes *Nature* **381** 678
[27] Timofeeva M, Bolshakov A, Tovee P D, Zeze D A, Dubrovskii V G and Kolosov O V 2016 Scanning thermal microscopy with heat conductive nanowire probes *Ultramicroscopy* **162** 42
[28] Minnich A J, Johnson J A, Schmidt A J, Esfarjani K, Dresselhaus M S, Nelson K A and Chen G 2011 Thermal conductivity spectroscopy technique to measure phonon mean free paths *Phys. Rev. Lett.* **107** 095901
[29] Mingo N and Broido D A 2005 Carbon nanotube ballistic thermal conductance and its limits *Phys. Rev. Lett.* **95** 096105
[30] Hu L, Desai T and Keblinski P 2011 Thermal transport in graphene-based nanocomposite *J. Appl. Phys.* **110** 033517
[31] Zhong H and Lukes J R 2006 Interfacial thermal resistance between carbon nanotubes: Molecular dynamics simulations and analytical thermal modeling *Phys. Rev.* B **74** 125403
[32] Chalopin Y, Volz S and Mingo N 2009 Upper bound to the thermal conductivity of carbon nanotube pellets *J. Appl. Phys.* **105** 084301
[33] Swartz E T and Pohl R O 1989 Thermal boundary resistance *Rev. Mod. Phys.* **61** 605
[34] Allen P B and Feldman J L 1993 Thermal conductivity of disordered harmonic solids *Phys. Rev.* B **48** 12581
[35] Schmidt A J, Collins K C, Minnich A J and Chen G 2010 Thermal conductance and phonon transmissivity of metal–graphite interfaces *J. Appl. Phys.* **107** 104907
[36] Koh Y K, Bae M-H, Cahill D G and Pop E 2010 Heat conduction across monolayer and few-layer graphenes *Nano Lett.* **10** 4363
[37] Wilson R B, Feser J P, Hohensee G T and Cahill D G 2013 Two-channel model for nonequilibrium thermal transport in pump-probe experiments *Phys. Rev.* B **88** 144305
[38] Osman M A and Srivastava D 2001 Temperature dependence of the thermal conductivity of single-wall carbon nanotubes *Nanotechnology* **12** 21
[39] Balandin A A, Ghosh S, Bao W, Calizo I, Teweldebrhan D, Miao F and Lau C N 2008 Superior thermal conductivity of single-layer graphene *Nano Lett.* **8** 902
[40] Collins P G and Avouris P 2000 Nanotubes for electronics *Sci. Am.* **283** 62
[41] Yu M-F, Lourie O, Dyer M J, Moloni K, Kelly T F and Ruoff R S 2000 Strength and breaking mechanism of multiwalled carbon nanotubes under tensile load *Science* **287** 637
[42] Chen J-H, Jang C, Ishigami M, Xiao S, Cullen W G, Williams E D and Fuhrer M S 2009 Diffusive charge transport in graphene on SiO_2 *Solid State Commun.* **149** 1080
[43] Wang H, Xu Y, Shimono M, Tanaka Y and Yamazaki M 2007 Computation of interfacial thermal resistance by phonon diffuse mismatch model *Mater. Trans.* **48** 2349
[44] Balandin A A 2011 Thermal properties of graphene and nanostructured carbon materials *Nat. Mater.* **10** 569
[45] Dubrovskii V G, Cirlin G E and Ustinov V M 2009 Semiconductor nanowhiskers: synthesis, properties, and applications *Semiconductors* **43** 1539